



## Particle entrainment and rotating convection in Enceladus' ocean

Ashley M. Schoenfeld<sup>1</sup><sup>✉</sup>, Emily K. Hawkins<sup>2</sup>, Krista M. Soderlund<sup>3</sup>, Steven D. Vance<sup>4</sup>, Erin Leonard<sup>4</sup> & An Yin<sup>1</sup>

Observations from Cassini have identified nanometer-sized silica grains in Saturn's E-ring although their origin is unclear. Tidal deformation within Enceladus' silicate core has been predicted to generate hot hydrothermal fluids that rise from the core-ocean boundary and traverse the subsurface ocean. This raises the possibility that the particles observed by Cassini could have been produced by hydrothermal alteration and ejected via the south polar plumes. Here, we use an analytical model to quantify potential for particle entrainment in Enceladus' ocean. We use scaling relations to characterize ocean convection and define a parameter space that enables particle entrainment. We find that both the core-ocean heat fluxes and the transport timescale necessary to drive oceanic convection and entrain particles of the observed sizes are consistent with observations and predictions from existing thermal models. We conclude that hydrothermal alteration at Enceladus' seafloor could indeed be the source of silica particles in Saturn's E-ring.

<sup>1</sup>Department of Earth, Planetary, and Space Sciences, University of California, Los Angeles, Los Angeles, CA 90095, USA. <sup>2</sup>Department of Physics, Loyola Marymount University, Los Angeles, CA 90045, USA. <sup>3</sup>Institute for Geophysics, Jackson School of Geosciences, The University of Texas at Austin, Austin, TX 78758, USA. <sup>4</sup>Jet Propulsion Laboratory, California Institute of Technology, Pasadena, CA 91109, USA. ✉email: [ashley.schoenfeld@ucla.edu](mailto:ashley.schoenfeld@ucla.edu)

Enceladus, a ~500-km-diameter moon of Saturn, is characterized by a highly tectonized surface<sup>1–3</sup> and ongoing venting of material from the south pole<sup>4</sup> sourced from a series of parallel “tiger-stripe” fractures in the ice shell. The tiger-stripe fractures act as conduits that cut through the ice shell, tapping into a sodium- and potassium-bearing subsurface liquid reservoir<sup>5–8</sup>. The detection of significant physical libration<sup>9</sup> further demonstrates that Enceladus’ outer ice shell is mechanically decoupled from its rocky core and suggests that the subsurface reservoir is a global ocean.

Subsequent chemical analyses of the south polar plumes with Cassini’s Cosmic Dust Analyzer (CDA) have revealed the presence of nanometer-scale silica particles, indicating that the water identified within the plumes was once in contact with silicate rock and subjected to high temperatures<sup>10,11</sup>. Consequently, the chemistry of Enceladus’ plumes has been interpreted as evidence for hydrothermal activity at the ocean/core interface. The identification of substantial amounts of H<sub>2</sub> in the plume likewise serves as a marker of hydrothermal processes, as the observed amount exceeds what would be expected from primordial storage or radiolysis<sup>12</sup>. The detection of silica grains in the plumes suggests that there are flows within the ocean capable of transporting materials from the core-ocean interface, through the ocean, and across the ice shell. The means by which oceanic flow within Enceladus could have realized the inferred transport, however, has not been fully addressed.

Fluid motions within Enceladus’ ocean may be driven by mechanical and/or thermal forcing. Mechanical forcing is most likely induced by the obliquity, libration, and/or eccentricity of Enceladus<sup>13</sup>. It is debated whether the small obliquity of Enceladus rules out its effectiveness as a flow-generating mechanism<sup>14–18</sup>. While physical libration could produce oceanic turbulent flows<sup>19,20</sup> and dominates tidally induced dissipation, the overall power dissipated in the ocean is nonetheless small<sup>21</sup>. However, tidal dissipation within the ice shell via eccentricity is often inferred to be a main source of tidal heating capable of maintaining a lasting global ocean inside Enceladus<sup>22</sup>. Furthermore, tidally induced deformation and friction within a porous silicate core may generate hot and narrow upwelling zones at the seafloor<sup>23</sup>, sourcing hot water into the cooler ocean layer<sup>24</sup>. The heat flux at the subsurface seafloor thus likely drives convection and mixing in the ocean<sup>25–29</sup>.

The suspension of particles in a fluid depends strongly on the mechanism of turbulence generation, namely buoyancy stresses driven by convection (viscous stress associated with buoyancy flux from the seafloor) or Reynolds stresses associated with unsteady turbulent motions (driven by convection or mechanical forcing)<sup>30,31</sup>. For rapidly rotating convection, such as expected for Enceladus’ ocean, thermally driven buoyancy forces are typically much larger than non-linear, inertial forces<sup>32</sup>. Moreover, experiments have shown that turbulent shear flows associated with downwelling cold plumes (surface cooling alone) were insufficient to cause entrainment, whereas entrainment occurred when heated from below<sup>30</sup>. These results are consistent with the ratio of Reynolds stresses to the weight per unit area of the particle,  $\Delta\rho g D$  (where  $\Delta\rho$  represents particle-fluid density difference,  $g$  is gravity, and  $D$  is particle diameter), being too small for incipient motion of a particle bed<sup>30</sup>. Convective entrainment is, therefore, argued to be the primary cause of upward transport of hydrothermal products, such as silica particles, from the ocean floor to the surface to be ejected at the south polar plumes. Thus, we consider only the role of thermal buoyancy stresses under the presence of rotation in transporting silica particles across the ocean of Enceladus. The geometry of such a fluid system is conceptualized in Fig. 1.

We apply a particle entrainment model based on laboratory experiments<sup>30,31</sup> (see “Methods”) and use scaling relations<sup>33–37</sup> (see “Methods”) to characterize length and velocity scales of

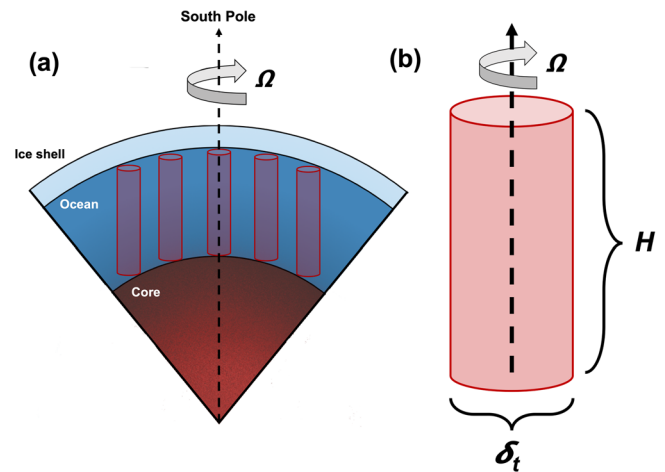


**Fig. 1 Rotationally dominated convection columns.** **a** Conceptual representation of rotationally dominated “Taylor” convection columns aligned with the axis of rotation within the ocean underneath Enceladus’ south polar terrain, and **b** simplified geometry of one such column.  $H$  represents the vertical length of the fluid system (in this case, the thickness of the ocean), and  $\delta_t$  represent the width of the column and depends on degree of thermal forcing. Not to scale: for a 60 km thick ocean, the Taylor columns are predicted to have widths of  $\delta_t \lesssim 1.6$  km.

**Table 1 Parameters for Enceladus’ ocean used in our calculations<sup>24,28,44,83</sup>.**

Parameter	Symbol	Value	Unit
Density contrast	$\Delta\rho$	1000	$\text{kg m}^{-3}$
		1200	
		2000	
Dynamic viscosity	$\eta$	$10^{-3}$	$\text{Pa s}$
Thermal expansion coefficient	$\alpha$	$1 \times 10^{-4}$	$\text{K}^{-1}$
		$5 \times 10^{-5}$	
		$1 \times 10^{-5}$	
Gravitational acceleration	$g$	0.113	$\text{m s}^{-2}$
Specific heat capacity	$c_p$	4200	$\text{J kg}^{-1} \text{K}^{-1}$
Thermal diffusivity	$\kappa$	$1.3 \times 10^{-7}$	$\text{m}^2 \text{s}^{-1}$
Viscous diffusivity	$\nu$	$10^{-6}$	$\text{m}^2 \text{s}^{-1}$
Thermal conductivity	$k$	0.5	$\text{W m}^{-1} \text{K}^{-1}$
Rotation rate	$\Omega$	$5.3 \times 10^{-5}$	$\text{rad s}^{-1}$
Ocean thickness	$H$	20	km
		40	
		60	

convection in the ocean using a parameter space constrained from the particle entrainment model results. Physical parameters for Enceladus’ ocean are summarized in Table 1.

## Results

Equation (1) (“Methods”) presents the ratio of buoyancy stress to weight per unit area of the particle; the condition for entrainment of solid particles with a density  $\rho_p$  in a thermally convecting fluid with a density  $\rho_f$  occurs when this ratio exceeds some critical value<sup>30,31</sup>. For the purposes of this study, we assume equilibrium in ocean composition and that thermal buoyancy dominates entrainment behavior. We algebraically solve for particle diameter with spherical geometry, determining its dependence on heat flux from the silicate core. Figure 2 illustrates the stability of predicted properties with depth and justify our decision to hold heat capacity and ocean density constant in our model. Contours are shown of density, thermal expansivity, and heat capacity vs. ocean

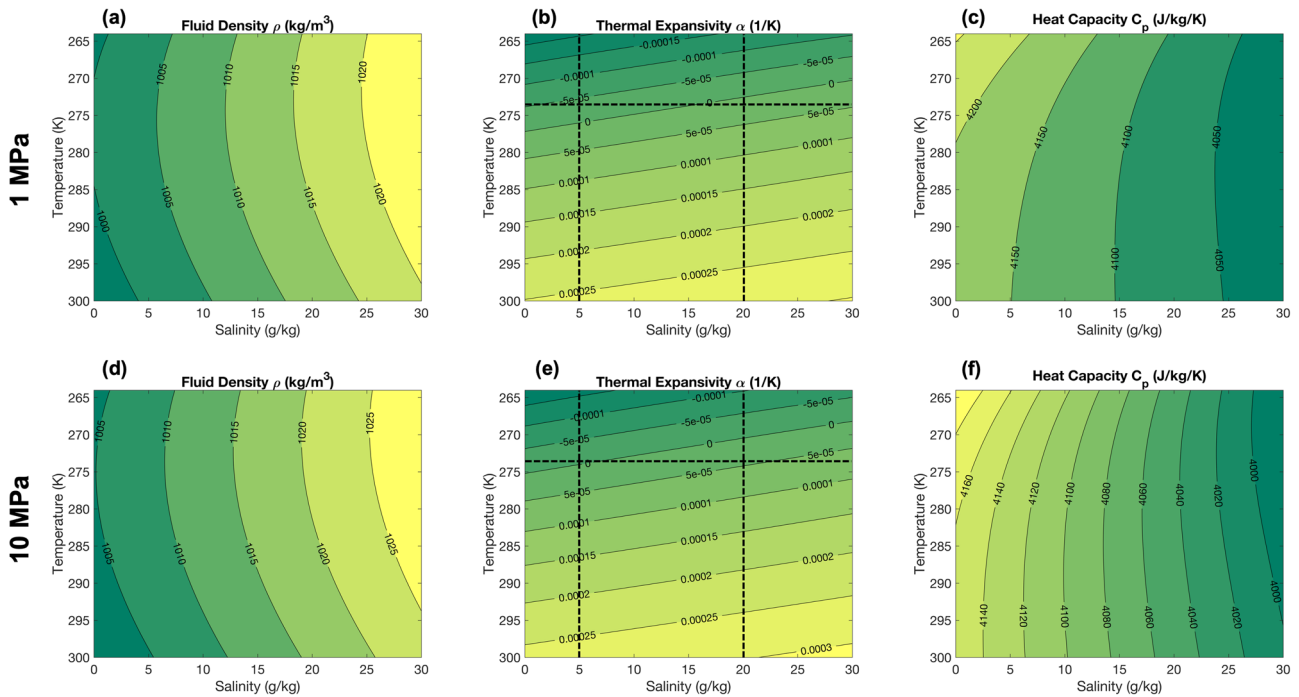


**Fig. 2** Contours of density, thermal expansivity, and heat capacity vs. ocean salinity and temperatures. Shown at pressures of 1 MPa (a–c) and 10 MPa (d–f). Black dashed lines indicate the lower and upper limits on ocean salinity based on in-situ observations made by Cassini<sup>6,42</sup>. For the ocean temperature, we assume 274 K<sup>44</sup>.

salinity and temperature at pressures of 1 and 10 MPa; ~1 MPa is approximately the pressure under 5 km of ice at the south pole, while 10 MPa is potentially 10's of km into the seafloor<sup>38</sup>. When calculating particle size, we assume that the thermal expansion coefficient is always positive so that convection may proceed throughout the ocean. As shown in Fig. 2b, positive buoyancy requires a minimum ocean salinity of ~20 g kg<sup>-1</sup>, or an increase in temperature by roughly half a degree to the point where the thermal expansivity again becomes positive. An ocean salinity of ~20 g kg<sup>-1</sup> is the higher end-member estimate for inferred plume salinity<sup>6</sup> but fits generally well within other estimates for ocean salinity<sup>10,39–44</sup>. As in previous studies, we assume a base temperature around 274 K<sup>44</sup> and assume  $\Delta T = 5$  mK in the normally adiabatic ocean<sup>38</sup>. Contour calculations were made specifying 12 g kg<sup>-1</sup> seawater to approximate the Cl rich ocean composition inferred from Cassini Dust Analyzer sampling of the plumes<sup>5</sup>.

We find that the entrained particle size increases with increasing core heat flux when assuming a constant thermal expansivity of  $\alpha = 1 \times 10^{-5} \text{ K}^{-1}$  (Fig. 3a). For a fixed heat flux, the entrained particle size increases with decreasing density contrast,  $\Delta\rho$ , between the particle and the fluid. Similarly, the relationship between the entrained particle size and heat flux varies with different thermal expansivity coefficients when assuming a constant density contrast of  $\Delta\rho = 1200 \text{ kg m}^{-3}$  (Fig. 3b); an order of magnitude change in thermal expansivity results in an order of magnitude change in estimated heat flux. For particles with silica density of  $2200 \text{ kg m}^{-3}$ <sup>10</sup>, we find that a heat flux of  $\geq 0.3 \text{ W m}^{-2}$  is necessary to explain entrainment of the largest detected particles.

We can compare the results of our particle entrainment model to the results from ref. 24. Their model shows that the distribution of heat flux along the seafloor is dominated by radially advecting water that varies laterally in temperature. These narrow upwellings are characterized as powerful hotspots, from 1 to 5 GW, with temperatures in excess of 363 K. For a core radius of ~190 km<sup>45</sup> and assuming that heat flux at the surface is confined to an area comparable in size to the modeled hotspots in ref. 24—

approximately 10% of the polar area—we estimate a heat flux of ~3 GW, which fits well into this 1–5 GW range. Reference 24 also predicts localized heat fluxes on the order of 1 to  $8 \text{ W m}^{-2}$ , averaged over a period of 10 Myr.

We calculate flow speeds (Eq. (5), “Methods”) in terms of the dimensionless free-fall Rossby number (i.e., the ratio of inertial to Coriolis forces) to be on the order of  $10^{-4}$  to  $10^{-3}$ , demonstrating the importance of rotation on convective transport. Figure 3c shows the turbulent length scale (“Methods”) versus heat flux. The range of heat fluxes reported above, based on observed plume particle sizes<sup>10</sup>, are highlighted by the yellow shaded area in Fig. 3c. Varying the ocean thicknesses  $H$  at 20 km, 40 km, and 60 km to accommodate the distribution of ice shell thickness variations<sup>9,16,45,46</sup> leads to turbulent length scales on the order of 100's of meters to a few kilometers. Figure 3d shows free-fall velocity versus heat flux.

Vertical flow speeds are on the order of a few  $\text{mm s}^{-1}$ , representing an upper bound. The corresponding transport time of entrained silica particles from the core-ocean boundary to the base of the ice shell can be estimated by  $T_{ff} = H/u_{ff}$ , which is on the order of several months and conversely represents a lower bound. Note that the length scale begins to plateau with increasing heat flux, suggesting that there is an upper bound on characteristic fluid length scale despite increasing heat flux. Conversely, there is also a minimum velocity, and by extension minimum length scale, that exists as heat is injected into the system.

Due to water's anomalous thermal expansion coefficient, there may exist a stably stratified layer in the upper ocean, extending from where the thermal expansion coefficient is negative at the freezing front to where the thermal expansion coefficient becomes positive such that convection proceeds. This layer provides a thermally conductive barrier between the convecting ocean and the ice and is similar to the stratified layer that has been hypothesized to exist in the ocean of Europa<sup>47</sup>. The fluid beneath the ice shell would be close to the temperature of water's zero thermal expansivity, or about 0.5 K above freezing for  $20 \text{ g kg}^{-1}$

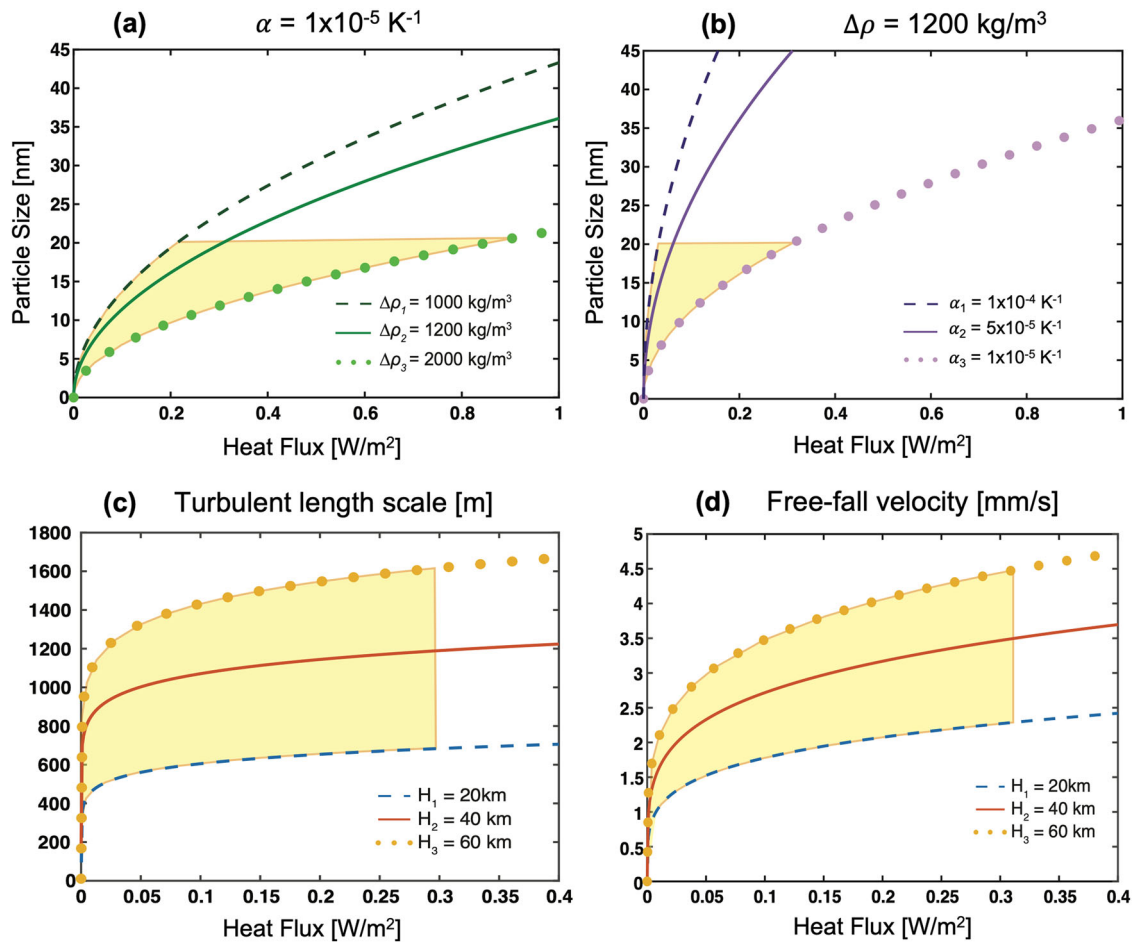


**Fig. 3 Particle size, length scale, and velocity results.** **a** Entrained particle size versus heat flux for three different fluid-particle density contrasts of  $\Delta\rho = 1000, 1200,$  and  $2000 \text{ kg m}^{-3}$  (corresponding to amorphous silica particle densities of  $2000, 2200,$  and  $3000 \text{ kg m}^{-3}$ , respectively) with a constant thermal expansion coefficient of  $\alpha \simeq 1 \times 10^{-5} \text{ K}^{-1}$ . **b** Entrained particle size versus heat flux for thermal expansion coefficients of  $\alpha \simeq 1 \times 10^{-5}, 5 \times 10^{-5},$  and  $1 \times 10^{-4} \text{ K}^{-1}$  with a constant density contrast of  $\Delta\rho = 1200 \text{ kg m}^{-3}$ . Yellow shaded areas represent the range of heat flux values that yield entrainment of particles comparable in size to those detected by Cassini and reported in ref. <sup>10</sup>. **c** Plot of turbulent length scale and **d** free-fall velocity versus heat flux for constant values of thermal expansivity ( $\alpha = 1 \times 10^{-5} \text{ K}^{-1}$ ) and density contrast ( $\Delta\rho = 1200 \text{ kg m}^{-3}$ ) within the ocean. Results for three different ocean thicknesses are also shown. Yellow shaded areas represent the range of heat flux values found in (a) and (b) for these  $\alpha$  and  $\Delta\rho$  values.

seawater at 1 MPa. For  $k = 0.5 \text{ W m}^{-1} \text{ K}^{-1}$ ,  $\Delta T_s \simeq \sim 0.5 \text{ K}$  (across the stagnant layer), and  $q = 0.3 \text{ W m}^{-2}$ , we use Eq. (6) (“Methods”) and calculate the equilibrium thickness of such a stagnant layer to be  $h_s \sim 1 \text{ m}$ . With no convection in the stratified layer, the vertical transport of tracers would be primarily achieved by diffusion with a timescale,  $\tau_{diff}$ , given by Eq. (7). For  $h_s = 1 \text{ m}$ , and  $\kappa = 1.3 \times 10^{-7} \text{ m}^2 \text{ s}^{-1}$ ,  $\tau_{diff} \sim 3$  months. However, ref. <sup>48</sup> estimates that vertical mixing through the stratified layer will take hundreds of years, provided mixing is dominated by molecular diffusivity. The difference in timescales comes from the difference in assumed heat flux; ref. <sup>48</sup> use an average global heat flux when calculating the stagnant layer thickness, whereas we use the heat flux under the south pole as inferred from our model. The two heat fluxes differ by an order of magnitude, resulting in a stagnant layer smaller by an order of magnitude, and resulting in a diffusive timescale smaller by three orders of magnitude. The thickness of a conducting stratified layer will likely vary with latitude; we argue that since heat flux is expected to be highest under the south pole, as supported by both observation and modeling, the thinnest possible section of such a layer would be found under the south pole. Reference <sup>48</sup> similarly explore the possibility that vertical mixing in the ocean may be enhanced by turbulence, induced either from libration or tidal dissipation. In such a scenario, molecular diffusivity would be

replaced by turbulent diffusivity, increasing both the depth of the stratified layer and the upward transport timescales, potentially increasing the diffusive timescale by three orders of magnitude. For the purposes of our study, we only invoke molecular diffusivity in our calculations, as the magnitude of turbulent diffusivity relevant to Enceladus is highly unconstrained.

We consider some alternate estimates for the ability of a rising particle to breach the stagnant layer. First, we suggest that the ability of an ascending plume to penetrate a stagnant layer can be estimated using the Brunt–Väisälä frequency (Eq. 8; “Methods”). Given sufficient upwelling momentum, a rising fluid parcel may overcome loss of buoyancy at the layer interface. For  $g = 0.113 \text{ m s}^{-2}$ ,  $\rho = 1000 \text{ kg m}^{-3}$ , and  $\frac{\partial \rho}{\partial z} \sim -5 \times 10^{-4} \text{ kg m}^{-3} \text{ m}^{-1}$ ,  $N \sim 0.24 \text{ mHz}$ , or a period of  $\sim 70 \text{ min}$ . Thus, a fluid parcel encountering the stagnant region needs a velocity of greater than  $0.24 \text{ mm s}^{-1}$  to traverse the boundary. In regions away from the south pole, the heat flux at the ice interface is likely about  $100\times$  lower, and the stagnant region would be proportionally thicker. As such, away from the south pole the necessary speed is likely closer to  $24 \text{ mm s}^{-1}$ . The characteristic vertical velocities we calculate (on the order of several  $\text{mm s}^{-1}$ ) thus imply that rising materials could reach the ice at the south pole where heat fluxes are high. Second, we consider Stokes dynamics for a vertically upwelling nanoparticle. Plugging in appropriate values into

Eq. (9), we calculate rise times that are on the order of nanoseconds and rise heights that are sub-atomic. Stokes dynamics are thus not expected to apply to nanometer-sized particles, such that Brownian motion is more appropriate. Consequently, further investigation is required to determine how such a stratified layer may affect material transport in Enceladus' upper ocean, as well as more consideration for boundary layer physics that may determine a particle's final transition from ocean to vacuum.

## Discussion

The new results we present for transport times through Enceladus' ocean have important differences from predictions made by other models. Reference <sup>10</sup> use the precipitation chemistry of silica to estimate transport times through and out of the ocean; the detected nano-silica particles with radii  $<10$  nm imply fast and continuous upward transport of hydrothermal products, likely within months to years. In contrast, ref. <sup>24</sup> use tidal dissipation models to predict that particles are carried from the seafloor to the bottom of the ice crust within a few weeks to months. Despite the differences in methodology, our calculations for transport times of several months are similar to lower end model predictions by ref. <sup>10</sup> and higher end predictions by ref. <sup>24</sup>. Ocean circulation models similarly predict vertical flow speeds of a few  $\text{mm s}^{-1}$  when driven by thermal convection, strongly constrained by rotation across the entire ocean domain<sup>28</sup>, again similar to our estimates. Our results imply that relatively fresh (i.e., more recently expelled) materials from hydrothermal vents (and possible biosignatures) are capable of being transported directly from the core to the south polar plumes and can be sampled and analyzed with a suitable instrument suite.

We note that while our assumed salinity is within previously estimated values, it is possible that salinity measurements inferred from direct plume sampling represent an underestimate of the ocean's bulk salinity. Heterogeneity in the thickness of Enceladus' ice shell suggests regions of localized freezing and melting exist at the ocean-ice interface, resulting in the modification of the density (and salinity) of the upper ocean via freshwater fluxes and brine rejection<sup>44</sup>. The ensuing low salinity layer could penetrate up to  $\sim 1$  km below the ocean-ice interface and would vary from the pole to the lower latitudes<sup>48,49</sup>. If such a layer were to have salinity below a critical point of about  $20 \text{ g kg}^{-1}$ , vertical transport of particles to the ice-ocean interface may be suppressed. If the upper part of Enceladus' ocean is stably stratified, for example, transit timescales may be on the order of hundreds of years<sup>50</sup>.

We now briefly address observational biases and potential consequences for our results. Salts, organics, and silica components have been identified within Saturn's E-ring and Enceladus' plumes via direct sampling and have been interpreted to originate as submicron particles floating below the icy crust, eventually serving as submicron condensation cores for the ice grains freezing out of plume ejecta<sup>51</sup>. The observed nanometer-sized silica particles from ref. <sup>10</sup> were initially embedded in icy grains and released as stream particles via sputter erosion in the E-ring; size estimates come from both integration of the Si+ signal and from dynamical analysis<sup>52</sup>. Stream-particle measurements offer the highest quality CDA spectra with the lowest possible signal contamination from refractory constituents, such as salt, that are otherwise prevalent in the E-ring and Enceladus' plume<sup>53</sup>. Stream particles are defined as nanometer-sized grains twice removed from the plume: they are particles that were able to escape from Enceladus plumes into the E-ring, were stripped down by plasma interactions, and subsequently ejected into interplanetary space at speeds of  $>100 \text{ km s}^{-1}$ <sup>52,53</sup>. Ultimately, however, the source of the Saturnian stream particles is Enceladus, and thus stream particles can be used to probe the moon's interior.

If we consider the hotspot heat fluxes of  $1\text{--}5 \text{ W m}^{-2}$  from ref. <sup>24</sup>, our model suggests that silica grains of  $\sim 100$  nanometers are capable of being entrained and transported to the ocean-core interface (see Fig. 3a, b). However, aside from the observed range of  $2\text{--}9$  nm radii particles, Cassini did not report larger silica grains. As discussed in ref. <sup>10</sup>, the size of a silica grain is controlled by its residency time within the ocean, as prescribed by thermo-chemical properties of a silica-water system. The argument for a hydrothermal origin for the silica nanoparticles is two-fold<sup>10</sup>: (1) the metal-poor (or metal-free) stream particle spectra<sup>54</sup> are not in agreement with those of typical rock-forming silicate minerals (that is, olivine or pyroxene), and (2) the improbability of homogeneous fragmentation of pure bulk silica into particles with radii exclusively below  $10$  nm within Enceladus. One may expect a broader continuum of sizing if the limiting factor was the ability to be ejected. It is possible then that larger nano-silica grains are not observed simply because they do not have time to grow beyond  $\sim 10$  nm. Alternatively, we posit that larger silica (or silicate) grains derived from other sources, i.e., abraded from the core, may be getting entrained and ejected, but that they result in grains that are too large to escape to altitudes where they could be fully characterized in the spectra.

Using the particle entrainment model, we show that the silica particle sizes observed by Cassini require core heat fluxes of  $\geq 0.3 \text{ W m}^{-2}$ , given our assumed values of thermal expansivity and density contrast. A summary schematic of our dynamical model for convective entrainment in Enceladus' ocean is presented in Fig. 4. If we assume that this heat flux is confined to  $\sim 10\%$  of the polar core area<sup>24</sup>, akin to hotspots, we estimate this heat flux to be  $\sim 3$  GW. Using the parameter space constrained from the particle entrainment model, we find that the turbulent length scale of Enceladus' ocean varies from  $100$ 's of meters to a few km, with vertical flow speeds on the order of  $\text{mm s}^{-1}$  that correspond to transport times of several months. Our derived values compare well to timescale predictions made by ref. <sup>10</sup> and ref. <sup>24</sup>. The analysis shows that convection in the ocean of Enceladus can explain the entrainment, transport, and ultimate delivery of silica particles from Enceladus' core/ocean interface to the ice shell. The physical mechanism proposed in this work can similarly be used to constrain material

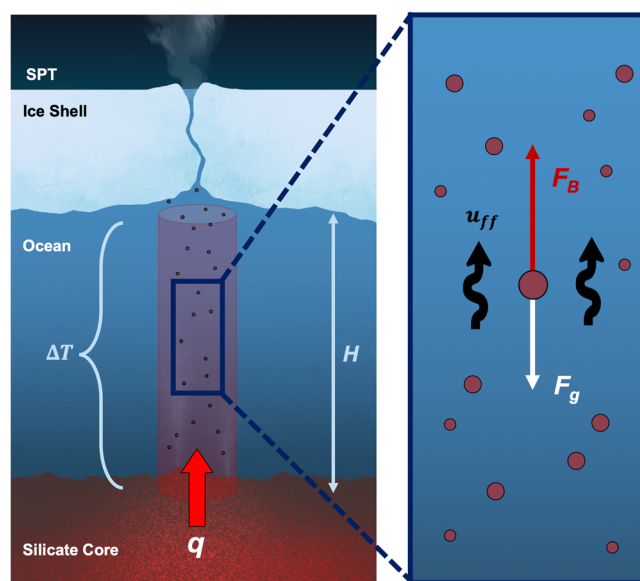


**Fig. 4** Particle entrainment in Enceladus' ocean. Conceptual diagram of a columnar vortex entraining particles in Enceladus' ocean (left). Conceptual diagram illustrating the force balance on an entrained silica particle that is traveling vertically upward at velocity  $u_{ff}$  (right).

mixing within other icy satellites with a three-layer internal structure comparable to that of Enceladus, where a silicate core is in contact with a subsurface ocean. Understanding the physical and chemical interactions between oceans, icy shells, and cores is central to determining the evolution of icy satellites, which in turn has implications for assessing the habitability of other ocean worlds.

## Methods

**Constraining particle size from convective upwelling.** The condition for entrainment of solid particles with a density  $\rho_p$  in a thermally convecting fluid with a density  $\rho_f$  occurs when the ratio of buoyancy stress to weight per unit area of the particle exceeds some critical value<sup>30,31</sup>:

$$\left(\frac{\eta\alpha gq}{c_p}\right)^{1/2} \frac{1}{\Delta\rho gD} \geq C \quad (1)$$

where  $C$  is an empirical constant with a value between 0.1 and 0.2,  $\Delta\rho = \rho_p - \rho_f$  is the density contrast between the solid particles and the fluid,  $\alpha$  is thermal expansivity of the fluid,  $\eta$  is fluid dynamic viscosity,  $q$  is basal heat flux,  $g$  is gravitational acceleration,  $D$  is particle diameter, and  $c_p$  is specific heat capacity.

The thermal expansion coefficient in (1) depends on pressure, temperature, and salinity. Observational inferences for the salinity of Enceladus' ocean remain uncertain, which translates to uncertainty in thermal expansivity. We choose three values of thermal expansivity for our calculations, adhering to the assumption that thermal expansivity is sufficiently positive such that Enceladus possesses a homogeneous and unstratified, convecting subsurface ocean:  $\alpha \simeq 1 \times 10^{-5}$ ,  $5 \times 10^{-5}$ ,  $1 \times 10^{-4} \text{ K}^{-1}$ . Our reasoning for these values is as follows: a thermal expansivity coefficient of  $1 \times 10^{-4} \text{ K}^{-1}$  is on the order of what has been used for Europa<sup>28,55</sup> yet is likely unrealistic for Enceladus given different pressure conditions. We also use the value  $5 \times 10^{-5} \text{ K}^{-1}$ , which is cited for Enceladus in ref. 44 given an ocean salinity of  $22 \text{ g kg}^{-1}$  and ocean temperature of  $274 \text{ K}$  at  $20 \text{ MPa}$ . This pressure is high for Enceladus, so we also use the value  $1 \times 10^{-5} \text{ K}^{-1}$ , which comes from calculations made with PlanetProfile at  $1 \text{ MPa}$  and  $10 \text{ MPa}$  for realistic salinity and temperature conditions within the ocean (Fig. 2)<sup>38</sup>. We use a dynamic viscosity of  $\eta \simeq 8.9 \times 10^{-4} \text{ Pa s}$ <sup>56</sup>, a thermal heat capacity at constant pressure of  $c_p \simeq 4200 \text{ J kg}^{-1} \text{ K}^{-1}$  (Fig. 2c, f), and the average gravitational acceleration for Enceladus,  $g \simeq 0.113 \text{ m s}^{-2}$ . For simplicity, we also assume that the difference in density between the silica grains and the convecting fluid,  $\Delta\rho$ , is constant throughout the ocean column, implying that the salinity of the water does not change significantly with depth (Fig. 2a, d), and that the density of the amorphous silica grains does not vary substantially.

**Length scales.** In a rotating, low viscosity fluid, buoyant upwellings can become influenced by the effects of rotation, which act to suppress and align plumes along the axis of rotation, creating columnar structures<sup>57–60</sup>. In this work, we assume oceanic flows will be sufficiently influenced by Enceladus' rotation such that fluid structures will be overall aligned with the axis of rotation. This assumption follows with recent work by ref. 28, though it is discussed therein that a low fluid thermal expansivity is likely needed to decrease the effects of buoyancy such that fluid remains organized in columnar-like structures. This finding additionally influences the range of ocean thermal expansivity values explored in this work (see above). Qualitatively, we thus describe the fluid as a series of vertical columns aligned with the axis of rotation<sup>61</sup>. The physical characteristics of the rotating system, such as the width of these columnar structures, depends on the strength of the rotation as well as the amount of energy entering the system<sup>62,63</sup>.

We define two end-member length scales of the convecting columns. For a viscosity-dominated system, the horizontal width of the columns ( $\delta_v$ ) may be written as<sup>64–66</sup>:

$$\delta_v \sim E^{1/3}H \quad (2)$$

where  $H$  is the total vertical length of the columns and is equivalent to the ocean thickness;  $E$  is the Ekman number defined by  $E = \frac{\eta}{2\rho\Omega H^2}$ , and  $\Omega$  is the rotational frequency (Fig. 1b). Using parameter values listed in Table 1, the Ekman number for Enceladus is  $\sim 10^{-12}$  to  $10^{-11}$ , corresponding to  $\delta_v$  on the order of 1 to 10 m. We also estimate the Rayleigh number for Enceladus, which represents the ratio between buoyancy and viscous and thermal diffusion in a fluid and is defined as  $Ra = \alpha g \Delta T H^3 / (\nu \kappa)$ . We use our range of thermal expansivities, ocean thicknesses, superadiabatic temperatures from (5), and a viscous diffusivity of  $\nu = 10^{-6} \text{ m}^2 \text{ s}^{-1}$  to find that  $Ra$  is on order of  $10^{17}$  to  $10^{19}$ . Taken together, these values suggest that the role of viscosity is not one of leading order<sup>28</sup>.

Conversely, for instances of strong thermal forcing, it is expected that inertia will instead play an important role in the dynamics of a rotating convective system. For inertia-dominated systems, the horizontal width of the turbulent convecting columns ( $\delta_t$ ) can be obtained by balancing the Coriolis and inertial forces<sup>67–69</sup>:

$$\delta_t \sim Ro^{1/2}H \quad (3)$$

where  $Ro = \frac{U}{2\Omega H}$  is the Rossby number representing the ratio of inertial to Coriolis forces with  $U$  as the characteristic velocity of the fluid. Today's most advanced numerical models are only just beginning to probe this turbulent regime, but ref. 70 find fluid structures that agree with (3) in the most rapidly rotating models containing strong thermal forcing. Furthermore, the recent study by ref. 37 finds that the viscous and turbulent length scales scale equivalently over the parameter space explored. Thus, we examine the turbulent scale as a function of heat flux in order to characterize the predicted length scale of our model flow.

**Flow velocities.** Rapidly rotating turbulent flows, which are thought to be relevant to the bulk convection of Enceladus' ocean, are governed by an inviscid balance between the system's rotation, inertia, and buoyancy<sup>28,37,71–73</sup>. Reference 74 shows that in a rapidly rotating system, the inertial timescale scales equivalently to the convective free-fall time. Thus, the characteristic system velocity can be estimated by the free-fall velocity, which is defined as  $u_{ff} \sim \sqrt{\alpha g H \Delta T}$ <sup>75–77</sup>. Here,  $\Delta T$  is the average superadiabatic temperature contrast across the convective layer.

We note that using the free-fall velocity to define the system scale velocity assumes a balance between buoyancy and inertia in the flow and assumes that viscous diffusion is negligible given that the inertia of the flow outweighs the viscous diffusion<sup>78,79</sup>. This will thus provide an upper bound on vertical velocity (and conversely a lower bound on transport timescale). We include a pre-factor of 0.1 in our calculations of free-fall velocity, as derived from convection experiments using water<sup>37,80</sup>. The free-fall velocity relates to the non-dimensional free-fall Rossby number,  $Ro_{ff}$ , by:

$$Ro_{ff} = \frac{u_{ff}}{2\Omega H} \approx \frac{(0.1)\sqrt{\alpha g H \Delta T}}{2\Omega H} \quad (4)$$

We note that this parameter is often referred to as the convective Rossby number.

Following refs. 80–82, we use the following scaling relationship to quantify heat transfer in the convecting system:

$$Nu \approx 0.15 Ra^{1.25} E^2 \quad (5)$$

where  $Nu = qH/(\rho_f c_p \kappa \Delta T)$  is the Nusselt number with  $\kappa$  representing thermal diffusivity. In addition,  $Ra$  is the Rayleigh number and  $E$  is the Ekman number. We use (5) to solve algebraically for the superadiabatic temperature and then plug it into our expression for free fall velocity.

**Penetrating a stagnant freshwater layer.** The low salinity of Enceladus' ocean implies the existence of a stratified freshwater layer just under the ice, due to water's anomalous thermal expansion. This layer provides a thermally conductive barrier between the convecting ocean and the ice<sup>47</sup>. We can use the heat diffusion equation to calculate the thickness of such a stagnant layer:

$$q = k \frac{\partial T}{\partial z} \approx k \frac{\Delta T_s}{h_s} \rightarrow h_s \approx \frac{k \Delta T}{q} \quad (6)$$

For  $k = 0.5 \text{ W m}^{-1} \text{ K}^{-1}$  (corresponding to a molecular diffusivity coefficient of  $\kappa = 1.3 \times 10^{-7} \text{ m}^2 \text{ s}^{-1}$ ), temperature across the stagnant layer  $\Delta T_s = 0.5 \text{ K}$ , and  $q = 0.3 \text{ W m}^{-2}$ , the thickness of such a stagnant layer would be  $h_s = 1 \text{ m}$ .

With no convection in the stratified layer, the vertical transport of heat would be primarily achieved by diffusion<sup>48</sup>:

$$\tau_{diff} \sim \frac{h_s^2}{\kappa} \quad (7)$$

For  $h_s = 1 \text{ m}$  and  $\kappa = 1.3 \times 10^{-7} \text{ m}^2 \text{ s}^{-1}$ ,  $\tau_{diff} \sim 3$  months.

Given sufficient momentum, an upwelling fluid parcel may breach this barrier layer. The vertical oscillation of a parcel at neutral density perturbed at the interface is given by the Brunt-Väisälä frequency<sup>61</sup>:

$$N = \sqrt{-\frac{g}{\rho} \frac{\partial \rho}{\partial z}} \quad (8)$$

For  $g = 0.113 \text{ m s}^{-2}$ ,  $\rho = 1000 \text{ kg m}^{-3}$ , and  $\frac{\partial \rho}{\partial z} \sim -5 \times 10^{-4} \text{ kg m}^{-3} \text{ m}^{-1}$  (calculated with Gibbs Seawater)<sup>38</sup>,  $N \sim 0.24 \text{ mHz}$ , or a period of  $\sim 70$  min. Thus, a parcel encountering the stagnant region needs a velocity of greater than  $0.24 \text{ mm s}^{-1}$  to traverse the boundary of  $\sim 1 \text{ m}$ .

Lastly, we consider an upward traveling nanometer scale particle subjected to Stokes resistance to provide an additional estimation for penetration timescale (see section S1 in Supplementary for detailed derivation). The rise time of the particle is given by:

$$t = \frac{m_p}{6\pi\mu r} \ln \left( 1 - \frac{6\pi\mu r}{m_p} \frac{\rho}{\Delta\rho g} v_0 \right) \quad (9a)$$

where  $m_p = 5.24 \times 10^{-20} \text{ kg}$  is the particle mass,  $r = 10 \text{ nm}$  is the particle radius,  $\rho = 2560 \text{ kg m}^{-3}$  is the particle density,  $\mu = 1 \text{ mPas}$  is the drag coefficient, and

$v_0 = 1 \text{ mm s}^{-1}$  is the initial upward velocity. The rise height is then given by:

$$h = (v_0 + v)t = \left( v_0 + \frac{m_p \Delta \rho g}{6\pi\eta r \rho} \left( 1 - e^{-\frac{6\pi\eta r t}{m_p}} \right) + v_0 e^{-\frac{6\pi\eta r t}{m_p}} \right) t \quad (9b)$$

With (9a) and (9b), we find the rise time to be measured in nanoseconds and the rise height to be sub-atomic. We therefore suggest that Stokes dynamics do not apply to particles of this size.

### Data availability

Data sharing not applicable to this article as no datasets were generated or analyzed during the current study. All model inputs are reported in Table 1.

### Code availability

Calculations for density, thermal expansivity, heat capacity, salinity for different temperature and pressure conditions for the ocean were made using The Gibbs SeaWater (GSW) Oceanographic Toolbox. The toolbox contains a comprehensive set of MATLAB routines based on the International Thermodynamic Equation of Seawater (TEOS-10). The code is free to download and available here: [https://www.teos-10.org/pubs/gsw/html/gsw\\_front\\_page.html](https://www.teos-10.org/pubs/gsw/html/gsw_front_page.html). MATLAB scripts were used to generate Fig. 3. These scripts can be provided by the corresponding author upon request.

Received: 20 April 2022; Accepted: 4 January 2023;

Published online: 10 February 2023

### References

- Helfenstein, P. & Porco, C. C. Enceladus' geysers: relation to geological features. *Astron. J.* **150**, 96 (2015).
- Bland, M. T., Singer, K. N., McKinnon, W. B. & Schenk, P. M. Enceladus' extreme heat flux as revealed by its relaxed craters. *Geophys. Res. Lett.* **39**, L17204 (2012).
- Crow-Willard, E. N. & Pappalardo, R. T. Structural mapping of Enceladus and implications for formation of tectonized regions. *J. Geophys. Res.* **120**, 928–950 (2015).
- Porco, C. C. et al. Cassini observes the active South Pole of Enceladus. *Science* **311**, 1393–1401 (2006).
- Postberg, F. et al. Sodium salts in E-ring ice grains from an ocean below the surface of Enceladus. *Nature* **459**, 1098–1101 (2009).
- Postberg, F., Schmidt, J., Hillier, J., Kempf, S. & Srama, R. A salt-water reservoir as the source of a compositionally stratified plume on Enceladus. *Nature* **474**, 620–622 (2011).
- Iess, L. et al. The gravity field and interior structure of Enceladus. *Science* **344**, 78–80 (2014).
- McKinnon, W. B. Effect of Enceladus' rapid synchronous spin on interpretation of Cassini Gravity. *Geophys. Res. Lett.* **42**, 2137–2143 (2015).
- Thomas, P. C. et al. Enceladus' measured physical libration requires a global subsurface ocean. *Icarus* **264**, 37–47 (2016).
- Hsu, H.-W. et al. Ongoing hydrothermal activities within Enceladus. *Nature* **519**, 207–210 (2015).
- Sekine, Y. et al. High-temperature water–rock interactions and hydrothermal environments in the chondrite-like core of Enceladus. *Nat. Commun.* **6**, 8604 (2015).
- Waite, J. H. et al. Cassini finds molecular hydrogen in the Enceladus Plume: evidence for hydrothermal processes. *Science* **356**, 155–159 (2017).
- Le Bars, M., Cébron, D. & Le Gal, P. Flows driven by libration, precession, and tides. *Annu. Rev. Fluid Mech.* **47**, 163–193 (2015).
- Chen, E. M. A. & Nimmo, F. Obliquity tides do not significantly heat Enceladus. *Icarus* **214**, 779–781 (2011).
- Chen, E. M. A., Nimmo, F. & Glatzmaier, G. A. Tidal heating in icy satellite oceans. *Icarus* **229**, 11–30 (2014).
- Beuthe, M., Rivoldini, A. & Trinh, A. Enceladus' and Dione's floating ice shells supported by minimum stress isostasy. *Geophys. Res. Lett.* **43**, 10–088 (2016).
- Matsuyama, I., Beuthe, M., Hay, H. C. F. C., Nimmo, F. & Kamata, S. Ocean tidal heating in icy satellites with solid shells. *Icarus* **312**, 208–230 (2018).
- Hay, H. C. F. C. & Matsuyama, I. Nonlinear tidal dissipation in the subsurface oceans of Enceladus and other icy satellites. *Icarus* **319**, 68–85 (2019).
- Rekier, J., Trinh, A., Triana, S. A. & Dehant, V. Internal energy dissipation in Enceladus' subsurface ocean from tides and libration and the role of Inertial Waves. *J. Geophys. Res.* **124**, 2198–2212 (2019).
- Wilson, A. & Kerswell, R. R. Can libration maintain Enceladus' ocean? *Earth Planet. Sci. Lett.* **500**, 41–46 (2018).
- Rovira-Navarro, M. et al. Do tidally-generated inertial waves heat the subsurface oceans of Europa and Enceladus? *Icarus* **321**, 126–140 (2019).
- Travis, B. J. & Schubert, G. Keeping Enceladus warm. *Icarus* **250**, 32–42 (2015).
- Roberts, J. H. The fluffy core of Enceladus. *Icarus* **258**, 54–66 (2015).
- Choblet, G. et al. Powering prolonged hydrothermal activity inside Enceladus. *Nat. Astron.* **1**, 841–847 (2017).
- Paluszkievicz, T., Garwood, R. & Denbo, D. Deep convective plumes in the Ocean. *Oceanography* **7**, 37–44 (1994).
- Legg, S., McWilliams, J. & Gao, J. Localization of deep ocean convection by a mesoscale Eddy. *J. Phys. Oceanogr.* **28**, 944–970 (1998).
- Legg, S. & McWilliams, J. C. Convective modifications of a geostrophic Eddy Field. *J. Phys. Oceanogr.* **31**, 874–891 (2001).
- Soderlund, K. M. Ocean dynamics of outer solar system satellites. *Geophys. Res. Lett.* **46**, 8700–8710 (2019).
- Amit, H. et al. Cooling patterns in rotating thin spherical shells—application to Titan's Subsurface Ocean. *Icarus* **338**, 113509 (2020).
- Solomatov, V. S., Olson, P. & Stevenson, D. J. Entrainment from a bed of particles by thermal convection. *Earth Planet. Sci. Lett.* **120**, 387–393 (1993).
- Lavorel, G. & Le Bars, M. Sedimentation of particles in a vigorously convecting fluid. *Phys. Rev. E* **80**, 046324 (2009).
- Schwaiger, T., Gastine, T. & Aubert, J. Force balance in numerical geodynamo simulations: a systematic study. *Geophys. J. Int.* **219**, S101–S114 (2019).
- Chandrasekhar, S. In *Hydrodynamic and Hydromagnetic Stability* (ed. Chandrasekhar, S.) 76–143 (Oxford University Press, 1961).
- Hide, R. & Mason, P. J. Sloping convection in a rotating fluid. *Adv. Phys.* **24**, 47–100 (1975).
- Grossmann, S. & Lohse, D. Multiple scaling in the ultimate regime of thermal convection. *Phys. Fluids* **23**, 045108 (2011).
- Cheng, J. S., Aurnou, J. M., Julien, K. & Kunnen, R. P. J. A heuristic framework for next-generation models of geostrophic convective turbulence. *Geophys. Astrophys. Fluid Dyn.* **112**, 277–300 (2018).
- Hawkins, E. K. et al. Laboratory models of planetary core-style turbulence. *Fluids* (in review).
- Vance, S. D. et al. Geophysical investigations of habitability in ice-covered ocean worlds. *J. Geophys. Res.* **123**, 180–205 (2018).
- Zolotov, M. Y. An oceanic composition on early and today's Enceladus. *Geophys. Res. Lett.* **34**, L23203 (2007).
- Zolotov, M. Y. & Postberg, F. Can nano-phase silica originate from chondritic fluids? The application to Enceladus' SiO<sub>2</sub> particles. in *Lunar and Planetary Science Conference Abstracts* Vol. 1777, 2496 (2014).
- Ingersoll, A. P. & Nakajima, M. Controlled boiling on Enceladus. 2. Model of the liquid-filled cracks. *Icarus* **272**, 319–326 (2016).
- Glein, C. R., Postberg, F. & Vance, S. D. In *Enceladus and the Icy Moons of Saturn* 39 (2018).
- Kang, W., Mittal, T., Bire, S., Campin, J. M. & Marshall, J. How does salinity shape ocean circulation and ice geometry on Enceladus and other icy satellites? *Sci. Adv.* **8**, 4665 (2022).
- Lobo, A. H., Thompson, A. F., Vance, S. D. & Tharimena, S. A pole-to-equator ocean overturning circulation on Enceladus. *Nat. Geosci.* **14**, 185–189 (2021).
- Čadež, O., Souček, O. & Běhoučková, M. Is Airy isostasy applicable to icy moons? *Geophys. Res. Lett.* **46**, 14299–14306 (2019).
- Hemingway, D. J. & Mittal, T. Enceladus' ice shell structure as a window on internal heat production. *Icarus* **332**, 111–131 (2019).
- Melosh, H. J., Ekholm, A. G., Showman, A. P. & Lorenz, R. D. The temperature of Europa's subsurface water ocean. *Icarus* **168**, 498–502 (2004).
- Zeng, Y. & Jansen, M. F. Ocean circulation on Enceladus with a high versus low salinity Ocean. *Planet. Sci. J.* **2**, 151 (2021).
- Kang, W. Different Ice-shell Geometries on Europa and Enceladus due to Their Different Sizes: Impacts of Ocean Heat Transport. *Astrophys. J.* **934**, 116 (2022).
- Kang, W., Marshall, J., Mittal, T. & Bire, S. Ocean dynamics and tracer transport over the south pole geysers of Enceladus. *Mon. Notices Royal Astron. Soc.* **517**, 3485–3494 (2022).
- Postberg, F. et al. The E-ring in the vicinity of Enceladus: II. Probing the moon's interior—the composition of E-ring particles. *Icarus* **193**, 438–454 (2008).
- Hsu, H. W. et al. Stream particles as the probe of the dust-plasma-magnetosphere interaction at Saturn. *J. Geophys. Res.* **116**, A09215 (2011).
- Kempf, S. et al. High-velocity streams of dust originating from Saturn. *Nature* **433**, 289–291 (2005).
- Postberg, F. et al. Discriminating contamination from particle components in spectra of Cassini's dust detector CDA. *Planet. Space Sci.* **57**, 1359–1374 (2009).
- Goodman, J. C., Collins, G. C., Marshall, J. & Pierrehumbert, R. T. Hydrothermal plume dynamics on Europa: implications for chaos formation. *J. Geophys. Res.* **109**, E3008 (2004).
- Johnson, J. W. & Norton, D. Critical phenomena in hydrothermal systems; state, thermodynamic, electrostatic, and transport properties of H<sub>2</sub>O in the critical region. *Am. J. Sci.* **291**, 541–648 (1991).

57. Greenspan, H. P. On the non-linear interaction of inertial modes. *J. Fluid Mech.* **36**, 257–264 (1969).
58. Zhong, F., Ecke, R. E. & Steinberg, V. Rotating Rayleigh–Bénard convection: asymmetric modes and vortex states. *J. Fluid Mech.* **249**, 135–159 (1993).
59. Julien, K., Knobloch, E. & Werne, J. A new class of equations for rotationally constrained flows. *Theor. Computat. Fluid Dyn.* **11**, 251–261 (1998).
60. Grooms, I., Julien, K., Weiss, J. B. & Knobloch, E. Model of convective Taylor columns in rotating Rayleigh–Bénard convection. *Phys. Rev. Lett.* **104**, 24501 (2010).
61. Tritton, D. J. In *Physical Fluid Dynamics* (ed. Tritton, D. J.) 162–182 (Clarendon, 1988).
62. Aurnou, J., Andreadis, S., Zhu, L. & Olson, P. Experiments on convection in Earth’s core tangent cylinder. *Earth Planet. Sci. Lett.* **212**, 119–134 (2003).
63. Panton, R. L. In *Incompressible Flow* (ed. Panton, R. L.) 772–825 (John Wiley & Sons, 2013).
64. Jones, C. A. Convection-driven geodynamo models. *Philos. Trans. Royal Soc. A* **358**, 873–897 (2000).
65. Zhang, K. & Schubert, G. Teleconvection: remotely driven thermal convection in rotating stratified spherical layers. *Science* **290**, 1944–1947 (2000).
66. Stellmach, S. & Hansen, U. Cartesian convection driven dynamos at low Ekman number. *Phys. Rev. E* **70**, 056312 (2004).
67. Hide, R. Jupiter and Saturn. *Proc. Math. Phys. Eng. Sci.* **336**, 63–84 (1974).
68. Ingersoll, A. P. & Pollard, D. Motion in the interiors and atmospheres of Jupiter and Saturn: scale analysis, anelastic equations, barotropic stability criterion. *Icarus* **52**, 62–80 (1982).
69. Cardin, P. & Olson, P. Chaotic thermal convection in a rapidly rotating spherical shell: consequences for flow in the outer core. *Phys. Earth Planet. Inter.* **82**, 235–259 (1994).
70. Guervilly, C., Cardin, P. & Schaeffer, N. Turbulent convective length scale in planetary cores. *Nature* **570**, 368–371 (2019).
71. Calkins, M., Julien, K., Tobias, S. & Aurnou, J. A multi-scale dynamo model driven by quasigeostrophic convection. *J. Fluid Mech.* **780**, 143–166 (2015).
72. Schwaiger, T., Gastine, T. & Aubert, J. Relating force balances and flow length scales in geodynamo simulations. *Geophys. J. Int.* **224**, 1890–1904 (2021).
73. Bire, S., Kang, W., Ramadhan, A., Campin, J. M. & Marshall, J. Exploring ocean circulation on icy moons heated from below. *J. Geophys. Res.* **127**, e2021JE007025 (2022).
74. Aurnou, J. M., Horn, S. & Julien, K. Connections between nonrotating, slowly rotating, and rapidly rotating turbulent convection transport scalings. *Phys. Rev. Res.* **2**, 43115 (2020).
75. Julien, K., Legg, S., McWilliams, J. & Werne, J. Rapidly rotating turbulent Rayleigh–Bénard convection. *J. Fluid Mech.* **322**, 243–273 (1996).
76. Horn, S. & Shishkina, O. Rotating non-Oberbeck–Boussinesq Rayleigh–Bénard convection in water. *Phys. Fluids* **26**, 55111 (2014).
77. Plumley, M. & Julien, K. Scaling laws in Rayleigh–Benard convection. *Earth Space Sci.* **6**, 1580–1592 (2019).
78. Chillà, F. & Schumacher, J. New perspectives in turbulent Rayleigh–Bénard convection. *Eur. Phys. J. E* **35**, 1–25 (2012).
79. Qiu, X. L. & Tong, P. Large-scale velocity structures in turbulent thermal convection. *Phys. Rev. E* **64**, 36304 (2001).
80. Soderlund, K. M., Schmidt, B. E., Wicht, J. & Blankenship, D. D. Ocean-driven heating of Europa’s icy shell at low latitudes. *Nat. Geosci.* **7**, 16–19 (2014).
81. Christensen, U. R. & Aubert, J. Scaling properties of convection-driven dynamos in rotating spherical shells and application to planetary magnetic fields. *Geophys. J. Int.* **166**, 97–114 (2006).
82. Gastine, T., Wicht, J. & Aubert, J. Scaling regimes in spherical shell rotating convection. *J. Fluid Mech.* **808**, 690–732 (2016).
83. Goodman, J. C. & Lenferink, E. Numerical simulations of marine hydrothermal plumes for Europa and other icy worlds. *Icarus* **221**, 970–983 (2012).

## Acknowledgements

We would like to thank Wanying Kang and two anonymous reviewers for their valuable comments and suggestions, which resulted in a greatly improved final manuscript. We would also like to thank Hamish Hay and Mohit Melwani Daswani for their valuable edits and inputs during the initial writing process. A.M.S. is supported by an NSF graduate student fellowship, grant number DGE-1650604. A portion of this research was carried out at the Jet Propulsion Laboratory, California Institute of Technology, under a contract with the National Aeronautics and Space Administration (80NM0018D0004).

## Author contributions

A.M.S. carried out the research and wrote the paper. E.K.H. and K.M.S. contributed ideas, offered valuable discussion, helped with theory, and contributed to writing. S.D.V. contributed ideas, helped with theory and calculations, and generated Fig. 3. E.L. and A.Y. contributed ideas and discussion.

## Competing interests

The authors declare no competing interests.

## Additional information

**Supplementary information** The online version contains supplementary material available at <https://doi.org/10.1038/s43247-023-00674-z>.

**Correspondence** and requests for materials should be addressed to Ashley M. Schoenfeld.

**Peer review information** *Communications Earth & Environment* thanks Wanying Kang and the other, anonymous, reviewer(s) for their contribution to the peer review of this work. Primary Handling Editors: João Duarte, Joe Aslin Peer reviewer reports are available.

**Reprints and permission information** is available at <http://www.nature.com/reprints>

**Publisher’s note** Springer Nature remains neutral with regard to jurisdictional claims in published maps and institutional affiliations.



**Open Access** This article is licensed under a Creative Commons Attribution 4.0 International License, which permits use, sharing, adaptation, distribution and reproduction in any medium or format, as long as you give appropriate credit to the original author(s) and the source, provide a link to the Creative Commons license, and indicate if changes were made. The images or other third party material in this article are included in the article’s Creative Commons license, unless indicated otherwise in a credit line to the material. If material is not included in the article’s Creative Commons license and your intended use is not permitted by statutory regulation or exceeds the permitted use, you will need to obtain permission directly from the copyright holder. To view a copy of this license, visit <http://creativecommons.org/licenses/by/4.0/>.

© The Author(s) 2023